Inorganic Chemistry

Article

pubs.acs.org/IC

Relationship between Torsion and Anisotropic Exchange Coupling in a Tb^{III}-Radical-Based Single-Molecule Magnet

Michael L. Baker,[†,‡] Takuya Tanaka,[†] Rina Murakami,[§] Seiko Ohira-Kawamura,[⊥] Kenji Nakajima,[⊥] Takayuki Ishida,[§] and Hiroyuki Nojiri*[,†]

[†]Institute for Materials Research, Tohoku University, Katahira, Sendai 980-8577, Japan

[§]Department of Engineering Science, The University of Electro-Communications, Chofu, Tokyo 182-8585, Japan

[⊥]Materials and Life Science Division, J-PARC Center, Japan Atomic Energy Agency, Tokai, Ibaraki 319-1195, Japan

Supporting Information

ABSTRACT: The incorporation of paramagnetic ligands within rare-earth ion clusters exhibiting large magnetic anisotropy has provided significant advancement in the design of single-molecule magnets (SMMs) with large blocking temperatures. However, the exchange interaction in such systems is complex and difficult to probe by conventional magnetometry techniques, and little is known about the structural relationships. Inelastic neutron scattering and terahertz electron paramagnetic resonance measurements are used complimentarily to investigate the large exchange interaction between a rare earth−radical pair in a Tb^{III}-based SMM complex. The origin of the exchange interaction is investigated for two molecular species in the crystallographic unit cell that exhibit different bonding structures between Tb^{III} and a 2pyNO radical. A correlation between the Tb−O−N−C torsion angles and the magnitudes of exchange couplings is found. Interestingly, a large nondegeneracy within the ground-state doublet is present for the larger torsion angle species. It is essential to consider the balance of two channels of exchange coupling, 2p−4f hybridization and 2p−5d charge transfer, to explain this characteristic behavior. The former channel gives the antiferromagnetic interaction, and the latter gives the ferromagnetic one. When an effective $\hat{J} = {}^1/_2$ Ising-type Hamiltonian is applied, the exchange couplings are evaluated to be antiferromagnetic $J^z = 9.89$ meV (79.8 cm^{-1}) for the low torsion angle (3.8°) species and $J^z = 7.39$ meV (59.6 cm^{-1}) for the larger torsion angle (15.8°) species. It is also found that a small percentage of the transverse exchange component must be included for the larger torsion angle to account for the observed nondegenerate ground state. The symmetry of the exchange couplings is discussed by considering the characters of d and f orbitals.

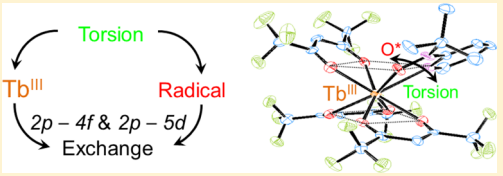

INTRODUCTION

The reduction of exchange-coupled magnetic systems to molecular-based units provides a convenient means to characterize the fundamental aspects of magnetic exchange with respect to the structural geometry and symmetry. Additionally, the reduction of the dimensionality introduces the possibility of investigating the magnetism in a regime where quantum fluctuations are enhanced. To this effect, molecular-based magnets have contributed to the investigation of a wide range of fundamental phenomena[1] such as spin frustration,[2−6] quantum tunneling of magnetization[7,8] and Néel vector tunneling,[9] quantum coherence,[10,11] and Berry phase interference.[12,13]

Given the finite number of exchange pathways between magnetic ions in molecular magnets (MMs), the exchange Hamiltonian can be treated exactly with little ambiguity. Inelastic neutron scattering (INS) has proven to be a very precise method to probe the detailed exchange correlations associated with exchange interactions in MMs.[14−17] Exchange-induced energy splitting can be probed directly by INS. Furthermore, the relative intensities of excitations and neutron momentum transfer give access to information about the wave functions of the involved states. INS has proven to be successful for testing empirical exchange Hamiltonians in a wide variety of metal ions of differing symmetries and electron occupation. Initial investigations concerned the simple case of spin−orbit-quenched 3d−3d transition-metal-ion exchange in dimer complexes.[18−21] The same approach was then extended to include the investigation of lanthanide (Ln), or rare earth, metal-ion-exchange interactions including mixed 3d−4f metal[22−26] and 4f−4f[27−32] systems. Exchange between free radicals and rare-earth metal ions has yet to be reported with the rigor applied to the other above-listed cases. This paper reports detailed spectroscopic analysis of the exchange mechanism between a radical and an anisotropic $4f^8$ ion, Tb^{III}. Understanding the nature of radical−lanthanide (R−Ln) exchange is of heightened relevance since the recent surge in Ln chemistry for the development of new single-molecule magnets (SMMs).[33−36] SMMs are a subclass of molecular complexes that exhibit a molecular-based bistability of magnetization below a blocking temperature and quantum tunneling of magnetization phenomena. The large anisotropic magnetic moments of Ln are well suited for the synthesis of SMMs with

Received: February 10, 2015
Published: May 26, 2015

DOI: 10.1021/acs.inorgchem.5b00300
Inorg. Chem. 2015, 54, 5732−5738

higher blocking temperatures. However, the compact nature of the 4f orbitals leads to very weak exchange interactions between Ln ions, relative to transition-metal-based SMMs, reducing the possibility of boosting blocking temperatures by ferromagnetic coupling of Ln ions. Recently, there has been considerable innovation to circumvent this issue by the development of free-radical-bearing ligands to enhance exchange interactions between Ln metal ions.[37−40] Furthermore, the highly anisotropic 4f moment and the isotropic radical spin may lead to new functionality. The strong anisotropy of 4f moments produces a metastability of the radical spin with which spin-coherent operation could be possible. Harnessing these properties could prove suitable for the design of new spin gates. For example, electric-current-induced spin-state switching within a terbium(III) phthalocyanine double-decker single-ion magnet (**TbPc$_2$**) absorbed onto a Au(111) surface has been demonstrated.[41] In this prototype system, it is manipulation of the free radical associated with a π orbital of the Pc ligand that is the active spin-switching site, which gives rise to a Kondo peak. Understanding R−Ln exchange and structural correlations is clearly of importance for the development of this research area.

The compact and highly anisotropic 4f orbitals of the Tb^{III} ion with respect to the diffuse isotropic 2p orbitals of a free radical lead to an asymmetric situation that can give rise to complex exchange terms such as Dzyaloshinski−Moriya interaction (DMI). Susceptibility measurements are particularly poor for the characterization of exchange in this situation because Ln crystal-field excitations and exchange-induced splitting often coexist in the same energy range. Interelectronic repulsion and spin−orbit coupling splits the $4f^n$ configuration into $^{2S+1}L_J$ energy levels. Each of these states is then further split by crystal-field perturbation. Previously, for the study of 3d−4f exchange, we developed a method using high-field high-frequency electron paramagnetic resonance (HF-EPR), which has enabled us to determine chemical trends in the strength of exchange interactions of various Ln^{III} ions with transition-metal ions using an Ising-type spin Hamiltonian interpretation.[42−45] In this study, complementary information provided by both INS and HF-EPR enable the development of this model to identify and treat mixing between low-energy eigenstates.

The selected compound is a Tb^{III} ($4f^8$) complex with paramagnetic ligand 2pyNO (*tert*-butyl 2-pyridyl nitroxide), $[Tb^{III}(hfac)_3(2pyNO)]$ (**Tb2pyNO**;[46] see Figure 1). Crystallographic analysis shows that there are two independent molecules in a unit cell. Both molecular species behave as SMMs. This leads to two activation energies (Δ) for the magnetization reversal, estimated as Δ/k_B = 39.2(3) K (7.0 meV) and 36(2) K (6.4 meV) determined by alternating-current susceptibility.[46] Dipolar fields between nearest-neighbor Tb ions are estimated to be on the order of a few microelectronvolts and are not effective. The coordination around the Tb ions makes an approximate square antiprism with seven O and one N atoms. The principal axis of the two Tb square antiprism moieties in the unit cell are tilted by 17.8° with respect to each other. The primary structural difference between the two molecular species in **Tb2pyNO** is the torsion angle Tb−O−N−C of the paramagnetic 2pyNO ligand (Table 1). It is proposed that this torsion angle is related to the exchange-coupling strength. INS and HF-EPR can be used to discriminate between the exchange couplings originating from the two different molecular species. Hence, the effect of the torsion angle on exchange within two chemically equivalent species can be conveniently investigated.

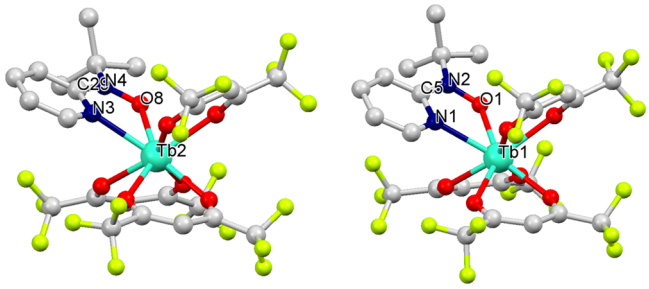

Figure 1. Crystallographic structures of the two independent molecular species (one, left; two, right) present within the unit cell of **Tb2pyNO**.

EXPERIMENTAL METHOD

INS experiments were performed at the Material and Life Science Facility, J-PARC. The direct geometry AMATERAS time-of-flight spectrometer[47] was used in a repetition rate multiplication (RRM) configuration probing four different dynamic ranges simultaneously. Two different RRM settings were used, providing spectra with incident neutron energies of (42.10, 15.17, 7.743, and 4.685) and (57.78, 18.24, 8.816, and 5.179) meV. The 7.743 and 8.816 incident neutron settings provide energy resolutions at the elastic line of and $\Delta E/E$ = 7.1 and 6.2%, respectively. A 1.2 g, 75% deuterated, polycrystalline sample of **Tb2pyNO** was prepared and contained inside a hollow aluminum canister for INS investigation. A closed-cycle refrigerator was used to maintain temperatures within a range from 3.8 to 40.0 K.

HF-EPR measurements were performed with the terahertz electron spin resonance apparatus (TESRA-IMR) installed in the magnetism division of the IMR, Tohoku University.[48] A solenoid magnet is fed by a 90 kJ capacitor bank, delivering a field pulse on the order of 25 ms in width. Applied fields of up to 30 T are generated. HF-EPR frequencies between 90 and 450 GHz were generated by backward-traveling wave oscillators and for frequencies greater than 450 GHz by an optically pumped far-infrared laser. HF-EPR absorption is measured by an InSb detector. A polycrystalline sample of **Tb2pyNO** was investigated in a He^4 cryostat between 4.2 and 40 K.

Analysis of the neutron scattering data was performed using Utsusemi.[49] Numerical simulations of EPR, magnetization, and INS were performed using *MATLAB* including *EasySpin*[50] toolboxes and *MAGPACK*.[51]

EXPERIMENTAL RESULTS AND ANALYSIS

Figure 2 shows the INS intensity as a function of energy and momentum transfer, $S(Q,E)$, measured with incident neutron settings of 7.743 and 8.816 meV measured at 3.8 K. The $S(Q,E)$ value includes scattering from several processes. Incoherent scattering from ligand atoms with large cross sections dominates the inelastic spectrum, characterized by their quadratic intensity dependence with respect to Q. Two magnetic excitations, centered at 3.7 and 4.9 meV (labeled as I and II, respectively), overlap with the incoherent scattering but are clearly identified at lower Q ranges. Intensities at energy transfer greater than II vary for the 7.743 and 8.816 meV settings; such a dependence on E_i signifies multiple elastic scattering of neutrons with the sample environment. Figure 3a shows INS energy spectra (E_i = 8.815 meV) for an integrated range of Q at 3.8 and 40 K. Incoherent scattering increases with increasing temperature, and two dominant intensities are identified at 1.75 and 2.45 meV in addition to a small incoherent feature centered at 4.4 meV between magnetic excitations I and II. With the slightly higher resolution setting (Figure 3b), the splitting of I into two unequal intensity excitations, labeled as Ia and Ib, is clearly resolved. The intensities of Ia and Ib are inequivalent at 3.8 K, but by 30.0 K, Ib reduces such that both Ia and Ib are equal in intensity. This temperature dependence suggests that Ib comes from

DOI: 10.1021/acs.inorgchem.5b00300
Inorg. Chem. 2015, 54, 5732−5738

Table 1. Selected Geometrical Parameters for Two Independent Molecules in the Crystal of Tb2pyNO (See Figure 1)

species one		species two	
	Bond Lengths (Å)		
Tb2−O8	2.357(6)	Tb1−O1	2.354(5)
O8−N4	1.298(7)	O1−N2	1.279(9)
N4−C29	1.405(10)	N2−C5	1.428(9)
C29−N3	1.348(10)	C5−N1	1.376(10)
Tb2−N3	2.530(6)	Tb1−N1	2.543(7)
Tb2−O_{hfac}	2.341(5)−2.374(5)	Tb1−O_{hfac}	2.320(5)−2.384(5)
	Bond Angles (deg)		
Tb2−O8−N4	124.5(5)	Tb1−O1−N2	127.1(4)
O8−N4−C29	118.2(6)	O1−N2−C5	118.2(6)
O8−Tb2−N3	62.40(19)	O1−Tb1−N1	62.68(17)
Tb2−N3−C29	119.2(5)	Tb1−N1−C5	119.3(5)
	Torsion Angles (deg)		
Tb2−O8−N4−C29	15.8(7)	Tb1−O1−N2−C5	3.8(7)
O8−N4−C29−N3	−0.8(8)	O1−N2−C5−N1	3.8(8)

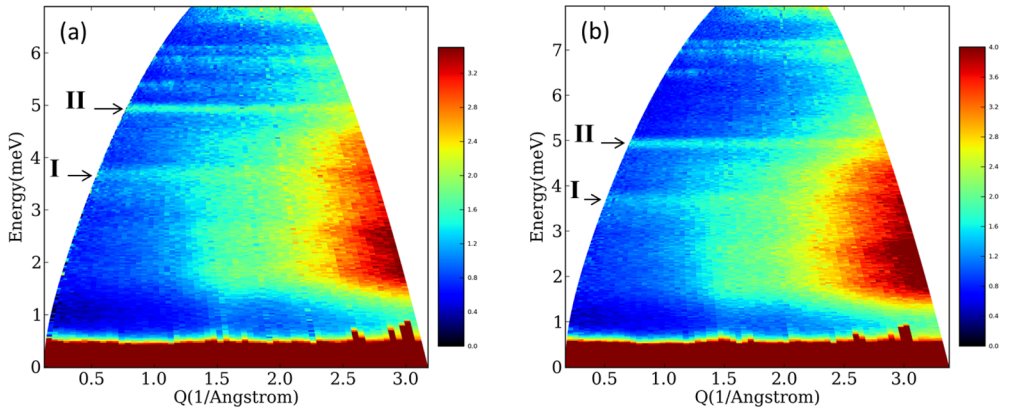

Figure 2. $S(Q,E)$ measured at 3.8 K with incident neutrons of E_i = 7.743 and 8.816 meV (a and b, respectively).

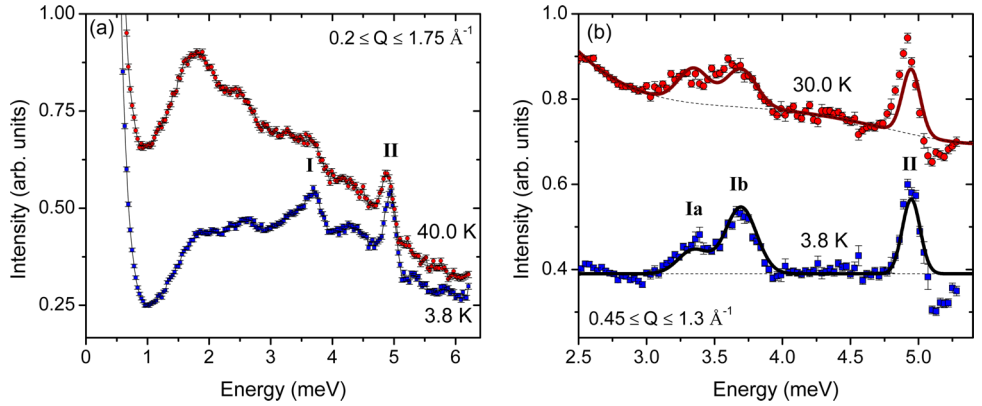

Figure 3. (a) Inelastic energy spectra measured at 3.8 and 40.0 K with incident neutrons of 8.816 meV (squares and circles, respectively). Magnetic excitations from **Tb2pyNO** species one and two are labeled. (b) Inelastic energy spectra measured at 3.8 and 30.0 K with incident neutrons of 7.743 meV (squares and circles, respectively, offset for clarity). Fine splitting of I is resolved, solid lines represent calculations based on Hamiltonian equation (1), and broken lines are fits of the nonmagnetic scattering intensity.

the ground state, while Ia comes from an excited state at 0.34 meV. The INS results gives the energy-level scheme presented in Figure 4. Taking advantage of the RRM configuration of AMATERAS enables a total dynamic range from 1 to 50 meV to be covered. However, no additional R−Ln exchange excitations or crystal-field excited states could be identified within this range.

The INS energy-level scheme is in direct agreement with HF-EPR. Figure 4 shows the frequency field plot for multifrequency HF-EPR measurements alongside the INS energy-level scheme. Two strong HF-EPR absorptions, labeled as α and β, are found to shift linearly to lower applied magnetic field with an increase of the HF-EPR frequency. The α absorption is slightly larger in intensity than β. Both absorptions are strongest at low temperature, indicating that they originate from resonances that come from the ground state (Figure 5). Together the temperature and field dependences indicate that the R−Ln exchange is antiferromagnetic because the field dependence of the resonances coming from the ground state decreases with increasing EPR frequency.[45]

Having not identified Tb crystal-field excitations up to energies of 50 meV by INS, it is a reasonable approximation to include only the

DOI: 10.1021/acs.inorgchem.5b00300
Inorg. Chem. 2015, 54, 5732−5738

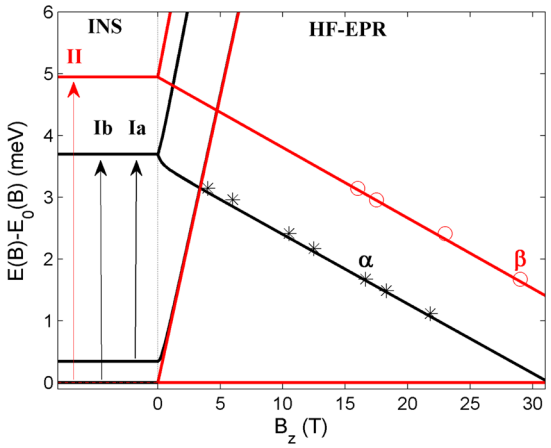

Figure 4. Combined INS energy-level scheme and HF-EPR frequency (1 meV = 241.8126 GHz) field diagram relative to the ground state. Arrows mark the observed INS excitations Ia, Ib, and II. Black stars mark the measured α resonances, and red circles mark the measured β resonances. Solid lines represent simulations based on eq 1.

ground-state $|J = 6, m_J = \pm 6\rangle$ pseudodoublet of Tb^{III} in the exchange Hamiltonian. The magnetic anisotropy can be written into the $\tilde{g}$ tensor such that only g_{zz} is nonzero. For Tb^{III}, $S = 3$, $L = 3$, $J = 6$, and $g = {}^3/_2$; hence, it can be expressed as $\hat{J} = {}^1/_2$ and $\tilde{g}_J^z = 18$. The exchange Hamiltonian is as follows:

$$\hat{H} = J^{iso}\hat{J}\cdot\hat{S} + J^z\hat{J}^z\hat{S}^z + d\hat{J}\times\hat{S} \quad (1)$$

where $\hat{S}$ is the spin half of the radical. The first two terms are the isotropic Heisenberg and anisotropic Ising exchange terms. The third term, DMI, introduces the off-diagonal elements to the total exchange matrix. In the applied magnetic field, the Zeeman effect on the Tb^{III} effective spin and the radial is added to Hamiltonian equation (1).

$$\tilde{g}_J^z\mu_B H\hat{J} + \tilde{g}_S\mu_B H\hat{S} \quad (2)$$

The exchange parameters J^{iso} and J^z can be simplified by the following relationships:

$$J^{iso} = Ar, \quad J^z = A(1 - |r|) \quad (3)$$

The parameter A is a scaling factor, and r describes the relative magnitude of J^{iso} and J^z. With these parameters, the Heisenberg model is described by $r = \pm 1$, the Ising model by $r = 0$, and the XY model by $r = -0.5$. Diagonalization of Hamiltonian equation (1) gives four eigenvalues with states described by linear combinations of the possible coupling permutations $|\downarrow,\uparrow\rangle$, $|\uparrow,\downarrow\rangle$, $|\downarrow,\downarrow\rangle$, and $|\uparrow,\uparrow\rangle$. In the Heisenberg limit, three eigenvalues are degenerate; in the Ising limit, two pairs of degenerate eigenvalues are obtained. The presence of DMI may also be responsible for breaking the degeneracy of the eigenvalues.

The INS results identify three separate excitations, and HF-EPR shows that at least two of these excited states exhibit Zeeman splitting. This number of exchange-induced energy splittings can be interpreted by taking into account the inclusion of two different exchange couplings for the two different molecular species within **Tb2pyNO**. This assumption is supported by the analysis presented in ref 46. For species one, the torsion angle is 15.8(7)°, and for species two, it is 3.8(7)° (see Table 1). The sensitivity of the torsion angle to the exchange strength is well reported for Gd^{III}–radical systems.[52,53] INS and HF-EPR are interpreted such that INS transition II and HF-EPR resonance β originate from one molecule and INS transitions Ia and Ib and HF-EPR resonance α originate from the other molecule. The larger intensity of α indicates larger mixing among Zeeman sublevels with respect to β. This is consistent with the INS results through the observed splitting between Ia and Ib with respect to II, which remains degenerate. The increased mixing between states involving transitions Ia, Ib, and α is driven by a structural reduction in the symmetry due to an increased torsion angle. Hence, we can conclude that the larger torsion angle in species one causes the signals Ia, Ib, and α and has a smaller exchange coupling.

To simplify the presence of nonunivocal parameter combinations, simulations are performed with DMI fixed to zero (solid lines in Figure 3b). The calculations reproduce INS transition II and HF-EPR resonance β in the pure Ising regime ($r = 0$ and $A = 9.89$ meV; Figure 4, red solid lines). A second set of parameters reproduce INS excitations Ia and Ib and HF-EPR resonance α and deviate significantly from the pure Ising situation because of the small but significant nonzero r term ($r = \pm 0.0493$ and $A = 7.04$ meV), which is responsible for mixing the ground-state doublet, giving rise to their observed nondegeneracy (Figure 4, black solid lines).

Figure 6 shows Zeeman diagrams calculated for species one and two separately. Labels indicate the observed INS (zero field) and 761 GHz EPR (in field) transitions. For both species, the EPR transition labeled with the green broken line is not experimentally observed, with measurements up to 50 K; despite theoretically having a nonzero transition intensity, the energy of this transition exceeds the 761 GHz maximum HF-EPR energy quanta probed. Transitions between states that are not labeled are associated with dynamics involving the Tb magnetic moment and, hence, a large change in M_J. HF-EPR probes the radical exchange coupling rather than the intramultiplet Zeeman splitting, and the resonances depend on the radical g value, with little sensitivity to the nature of the Tb^{III} effective g values. The $\Delta S = \pm 1$ transition is optically forbidden; hence, the observation by HF-EPR of

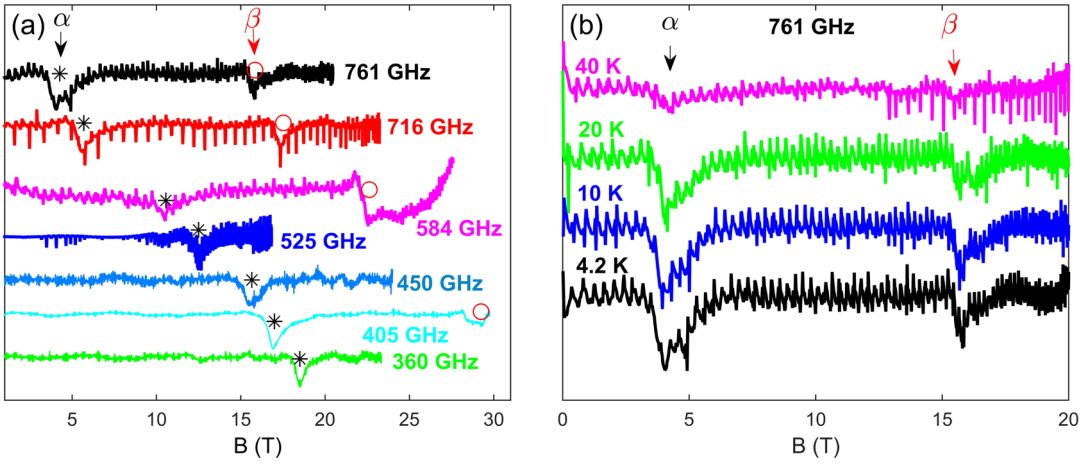

Figure 5. (a) HF-EPR measured at 4.2 K for various frequencies. (b) Temperature dependence of 761 GHz HF-EPR spectra. Labels α and β mark the positions of the measured resonances in the applied magnetic field.

DOI: 10.1021/acs.inorgchem.5b00300
Inorg. Chem. 2015, 54, 5732–5738

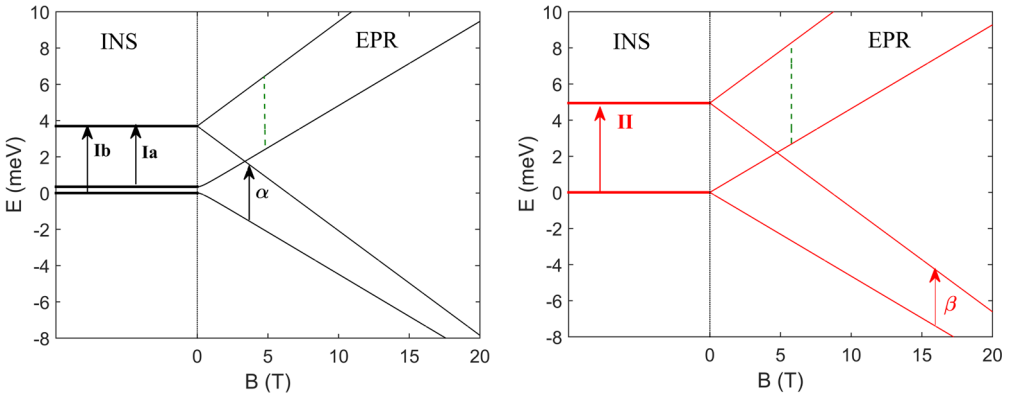

Figure 6. Calculated Zeeman diagrams for species one (left) and two (right). Solid arrow annotations label observed INS and 761 GHz EPR transitions. The green broken line labels the experimentally inaccessible excited-state resonance.

these transitions implies that rotational symmetry in the spin space is broken, and S is not a good quantum number. Simulations fit HF-EPR data with radical g values 1.92 and 1.97 for species one and two, respectively (Figure S3 in the Supporting Information, SI). The effective Tb^{III} doublet $\tilde{g}_j^z$ is fixed to 18. To simulate INS spectra, simulations for each set of parameters are summed together in a 1:1 ratio, reproducing the correct relative intensity contributed from both molecules (Figure 3b). The same procedure is used to simulate HF-EPR spectra, magnetic susceptibility, and magnetization (see the SI). Additional details of the INS and HF-EPR simulations can be found in the SI.

DISCUSSION

The **Tb2pyNO** SMM reveals several interesting structural relationships relative to its magnetic properties and underlying energy-level composition. Similar to the sandwich-type ligand geometry of the **$TbPc_2$** complexes, the **Tb2pyNO** Tb^{III} is eight-coordinate, forming an approximate compressed square antiprism.[54] For Tb^{III}, this geometry favors the oblate angular dependence of the $m_j = \pm 6$ charge density, while other m_j states exhibit prolate densities.[34] This contrast has been shown to lead to very large separations between $m_j = \pm 6$ and the first excited state for such structurally compressed Tb^{III} clusters. No evidence of excited states was identified by cold source neutron INS, probing a maximum energy transfer on the order of 400 cm^{-1} (~50 meV). Given the molecular geometry, an energy separation of such magnitude is quite plausible; however, the possibility of high-energy excited states being masked by strong scattering coming from lattice vibrations cannot be ruled out.

Given the energetic isolation of the $m_j = \pm 6$ states with respect to the excited states, the effective doublet Hamiltonian equation (1) is appropriate to precisely reproduce the INS and HF-EPR results. Putting together the information from both INS and HF-EPR gives detailed insight into the **Tb2pyNO** energy-level scheme. This enables a clear distinction between the two molecular species present within the unit cell. The torsion angle of the paramagnetic ligand and Tb^{III} is thought to be responsible for the differences in the magnetic properties of molecular species one (torsion angle 15.8°) and two (torsion angle 3.8°). Other than being the primary structural difference between the two species present, the effect of torsion has already been shown to correlate with exchange for Gd−radical systems. The orbitally quenched nature of Gd^{III} has made it a prototype system to understand Ln magnetism. Recent analysis of Gd−radical structural correlations shows that torsion correlates with the strength and sign of the coupling.[52,53] Density functional theory calculations of dimeric Gd^{III} complexes with N_2^{3-} radical bridging ligands have shown the mechanism for strong antiferromagnetism to be via direct 2p−4f hybridization.[55] Calculations performed for various N−Gd−N−Gd−N torsion angles found that the magnitude of antiferromagnetic exchange decreases with increasing torsion angle. In the large torsion angle limit, an overall ferromagnetic Gd−radical exchange is obtained. Ferromagnetic Gd−radical exchange can be understood to be equivalent to the Gd−Cu model developed by Kahn et al.[56] The mechanism proposed is that the radical π^* overlaps with an empty Gd 5d orbital, giving rise to a 2p to 5d electron-transfer-based ferromagnetic exchange interaction. As the torsion angle increases, the radical π^* nodal plane displaces with respect to the Gd 5d basal plane corresponding to enhanced orbital 2p−5d hybridization, increasing the ferromagnetic exchange strength.

The sign and magnitude of the net exchange between Gd−radical complexes are hence a combination of 2p−5d and 2p−4f contributions, introducing ferromagnetic and antiferromagnetic components to the net interaction, respectively. An increase of the radical torsion angle increases 2p−5d overlap and decreases 2p−4f overlap. Unlike Gd^{III}, Tb^{III} requires knowledge of the nature of the anisotropy in addition to the sign and magnitude of the exchange interaction. Some previous studies have attempted to rationalize Ln−radical exchange for ions other than Gd^{III} by bulk magnetic measurements.[57,58] However, in contrast to previous investigations, which were based on bulk magnetic susceptibility results, this work applies detailed spectroscopic probes to precisely characterize the exchange interaction within a simplified effective Hamiltonian model. On the basis of the extensive Gd−radical evidence, it is reasoned that the **Tb2pyNO** species one with the larger 15.8(7)° torsion angle exhibits a weaker net antiferromagnetic exchange strength than the species two molecule with a torsion angle of just 3.8(7)°. However, we also observe that the increase in torsion introduces a splitting within the ground-state doublet, signifying a change in the symmetry of the exchange in addition to the magnitude. It is found that a weak non-Ising component, introduced to the exchange matrix via nonzero r, can explain the observed splitting. Full analysis of the origin of the splitting is most clearly understood within the effective model by writing out Hamiltonian equation (1) in terms of the net exchange matrix, which including DMI is

DOI: 10.1021/acs.inorgchem.5b00300
Inorg. Chem. 2015, 54, 5732−5738

$$\hat{H} = \hat{J}\cdot\begin{pmatrix} J_{xx} & d_z & -d_y \\ -d_z & J_{yy} & d_x \\ d_y & -d_x & J_{zz} \end{pmatrix}\cdot\hat{S} \quad (4)$$

Splitting of the ground-state doublet in **Tb2pyNO** species one can be introduced by $J_{xx} = J_{yy} \neq 0$ (i.e., nonzero r in eq 3) or equivalency via DMI by nonzero d_z and $-d_z$. The requirement to introduce such an exchange term of different symmetry in going from a 3.8 to 15.8° torsion angle signifies the switching-on of 2p−5d Tb−radical charge transfer. Positive J_{xx} and J_{yy} (nonzero r) is consistent with the Kahn model for explaining ferromagnetism in Gd−Cu systems. However, we also find that HF-EPR and INS can be equivalently reproduced for species one with $d_z = \pm 0.338$ meV, $J_{zz} = 7.04$ meV, and $J_{xx,yy} = 0$. In either case, the required change of symmetry to the exchange matrix with respect to torsion implies a significant change in the balance of the 4f and 5d exchange channels.

It is worth comparing the magnitude of the Tb−radical exchange interaction with the Gd^{III}-substituted molecule **Gd2pyNO**.[52] All molecules within the **Gd2pyNO** unit cell are identical with a Gd−O−C−N torsion angle of 19.5°. An antiferromagnetic exchange interaction of 1.19 meV is determined with a $\hat{H} = J^{iso}\hat{J}_{Gd}\hat{S}$ Hamiltonian, where $\hat{J}_{Gd} = {}^{7}/_{2}$. To compare the magnitude of this exchange constant with that of the Tb analogue, differences in the Hamiltonians due to the Tb effective $\hat{J} = {}^{1}/_{2}$ model must be considered. The magnitude of exchange constants J^z are a factor of 12 greater than the values derived by coupling the full $\hat{J} = 6$ operator, i.e., $J^z/12 = 0.62$ and 0.82 meV. These **Tb2pyNO** exchange constants are somewhat less than the **Gd2pyNO** value, which is consistent with the chemical trend found for Ln−Cu exchange interactions.[59]

CONCLUSION

The detailed spectroscopic investigation of the **Tb2pyNO** SMM reveals strong antiferromagnetic Tb^{III}−radical exchange interactions. Two molecular species present within the crystal result in significantly different exchange interactions because of differences in the 2pyNO paramagnetic ligand torsion angle. Large exchange splitting energies of 3.7 and 4.9 meV are determined to correspond to 2pyNO ligand torsion angles of 15.8° and 3.8°, respectively. Probing such energies requires HF-EPR at near-terahertz frequencies and cold-source INS. The complementary analysis of HF-EPR and INS discriminates between the spectral contributions of the two molecular species present within **Tb2pyNO**. Analysis concludes that a small torsion angle (3.8°) results in pure antiferromagnetic exchange interpreted within an effective Ising-type Hamiltonian model [$\hat{H} = J^z\hat{J}^z\hat{S}^z$, where $J^z = 9.89$ meV (79.8 cm^{-1})]. The mechanism of this interaction is proposed to be via direct 2p−4f overlap.

Increased torsion (15.8°) results in an overall reduction in the antiferromagnetic exchange strength. Additionally, INS results determine that the ground-state doublet becomes nondegenerate in zero field for the larger torsion angle species. The nondegeneracy is reasoned to be due to the emergence of exchange of different symmetry, via 2p−5d charge transfer. The larger torsion angle is proposed to increase radical π^* nodal plane displacement with respect to the Tb^{III} 5d basal plane, introducing a small yet significant 2p−5d hybridization. Adding a small ferromagnetic Heisenberg contribution to the dominant antiferromagnetic Ising-type Hamiltonian mixes the doublet states, reproducing the observed nondegeneracy [$\hat{H} = J^{iso}\hat{J}\cdot\hat{S} + J^z\hat{J}^z\hat{S}^z$, where $J^{iso} = -0.347$ meV (-2.8 cm^{-1}) and $J^z = 7.39$ meV (59.6 cm^{-1})]. Unlike isotropic Gd^{III}, the strong Ising-type anisotropy of Tb^{III} enables the contributions to the interaction, originating from 2p−4f and 2p−5d hybridization, to be separated out, unraveling the overall contributions to the net exchange with respect to the torsion angle. This work contributes to the understanding of exchange between a radical and a rare-earth ion and is of interest for the interpretation of R−Ln SMM magnetism. Mixing within the ground-state doublet is found to be sensitive to the torsion angle, via an underlying correlation with 2p−5d and 2p−4f channels of exchange interaction, which has direct implications on the blocking temperature in Ln−R SMMs.

ASSOCIATED CONTENT

Supporting Information

Additional HF-EPR results, magnetization data, and additional details relating to simulations. The Supporting Information is available free of charge on the ACS Publications website at DOI: 10.1021/acs.inorgchem.5b00300.

AUTHOR INFORMATION

Corresponding Author

*E-mail: nojiri@imr.tohoku.ac.jp.

Present Address

‡Department of Chemistry, Stanford University, Stanford, CA 94305.

Notes

The authors declare no competing financial interest.

ACKNOWLEDGMENTS

This work was performed under the Inter-University Cooperative Research Program of the Institute for Materials Research, Tohoku University. Experiments were carried out using the AMATERAS time-of-flight neutron spectrometer with the approval of J-PARC (Grant 2012B0251). M.L.B. thanks the Japan Society for the Promotion of Science for a postdoctoral fellowship.

REFERENCES

(1) Furrer, A.; Waldmann, O. *Rev. Mod. Phys.* **2013**, *85*, 367−420.
(2) Gatteschi, D.; Pardi, L.; Barra, A. L.; Müller, A.; Döring, J. *Nature* **1991**, *354*, 463.
(3) Chiorescu, I.; Wernsdorfer, W.; Müller, A.; Bögge, H.; Barbara, B. *Phys. Rev. Lett.* **2000**, *84*, 3454−3457.
(4) Cador, O.; Gatteschi, D.; Sessoli, R.; Larsen, F. K.; Overgaard, J.; Barra, A.-L.; Teat, S. J.; Timco, G. A.; Winpenny, R. E. P. *Angew. Chem., Int. Ed.* **2004**, *43*, 5196.
(5) Garlea, V. O.; Nagler, S. E.; Zarestky, J. L.; Stassis, C.; Vaknin, D.; Kögerler, P.; McMorrow, D. F.; Niedermayer, C.; Tennant, D. A.; Lake, B.; Qiu, Y.; Exler, M.; Schnack, J.; Luban, M. *Phys. Rev. B* **2006**, *73*, 024414.
(6) Baker, M. L.; et al. *Proc. Natl. Acad. Sci. U.S.A.* **2012**, *109*, 19113.
(7) Friedman, J. R.; Sarachik, M. P.; Tejada, J.; Ziolo, R. *Phys. Rev. Lett.* **1996**, *76*, 3830−3833.
(8) Thomas, L.; Lionti, F.; Ballou, R.; Gatteschi, D.; Sessoli, R.; Barbara, B. *Nature* **1996**, *383*, 145.
(9) Waldmann, O.; Stamatatos, T. C.; Christou, G.; Güdel, H. U.; Sheikin, I.; Mutka, H. *Phys. Rev. Lett.* **2009**, *102*, 157202.
(10) Carretta, S.; Santini, P.; Amoretti, G.; Guidi, T.; Copley, J. R. D.; Qiu, Y.; Caciuffo, R.; Timco, G.; Winpenny, R. E. P. *Phys. Rev. Lett.* **2007**, *98*, 167401.

DOI: 10.1021/acs.inorgchem.5b00300
Inorg. Chem. 2015, 54, 5732−5738

(11) Bertaina, S.; Gambarelli, S.; Mitra, T.; Tsukerblat, B.; Muller, A.; Barbara, B. *Nature* **2008**, *453*, 203.
(12) Wernsdorfer, W.; Sessoli, R. *Science* **1999**, *284*, 133−135.
(13) Ramsey, C. M.; del Barco, E.; Hill, S.; Shah, S. J.; Beedle, C. C.; Hendrickson, D. N. *Nat. Phys.* **2008**, *4*, 277.
(14) Basler, R.; Boskovic, C.; Chaboussant, G.; Gl, H. U.; Murrie, M.; Ochsenbein, S. T.; Sieber, A. *Chem. Phys. Chem.* **2003**, *4*, 901−901.
(15) Baker, M. L.; Mutka, H. *Eur. Phys. J.: Spec. Top.* **2012**, *213*, 53−68.
(16) Baker, M. L.; Guidi, T.; Carretta, S.; Ollivier, J.; Mutka, H.; Güdel, H. U.; Timco, G. A.; McInnes, E. J. L.; Amoretti, G.; Winpenny, R. E. P.; Santini, P. *Nat. Phys.* **2012**, *8*, 906.
(17) Mourigal, M.; Fuhrman, W. T.; Sheckelton, J. P.; Wartelle, A.; Rodriguez-Rivera, J. A.; Abernathy, D. L.; McQueen, T. M.; Broholm, C. L. *Phys. Rev. Lett.* **2014**, *112*, 027202.
(18) Furrer, A.; Güdel, H. U. *Phys. Rev. Lett.* **1977**, *39*, 657−660.
(19) Güdel, H. U.; Furrer, A. *Mol. Phys.* **1977**, *33*, 1335.
(20) Guedel, H. U.; Stebler, A.; Furrer, A. *Inorg. Chem.* **1979**, *18*, 1021−1023.
(21) Furrer, A.; Güdel, H. U. *J. Magn. Magn. Mater.* **1979**, *14*, 256.
(22) Aebersold, M. A.; Güdel, H. U.; Hauser, A.; Furrer, A.; Blank, H.; Kahn, R. *Phys. Rev. B* **1993**, *48*, 12723−12731.
(23) Dreiser, J.; et al. *Chem. Sci.* **2012**, *3*, 1024−1032.
(24) Klokishner, S. I.; Ostrovsky, S. M.; Reu, O. S.; Palii, A. V.; Tregenna-Piggott, P. L. W.; Brock-Nannestad, T.; Bendix, J.; Mutka, H. *J. Phys. Chem. C* **2009**, *113*, 8573−8582.
(25) Kofu, M.; Yamamuro, O.; Kajiwara, T.; Yoshimura, Y.; Nakano, M.; Nakajima, K.; Ohira-Kawamura, S.; Kikuchi, T.; Inamura, Y. *Phys. Rev. B* **2013**, *88*, 064405.
(26) Kettles, F. J.; Milway, V. A.; Tuna, F.; Valiente, R.; Thomas, L. H.; Wernsdorfer, W.; Ochsenbein, S. T.; Murrie, M. *Inorg. Chem.* **2014**, *53*, 8970−8978.
(27) Furrer, A.; Güdel, H. U.; Blank, H.; Heidemann, A. *Phys. Rev. Lett.* **1989**, *62*, 210−213.
(28) Furrer, A.; Güdel, H. U.; Krausz, E. R.; Blank, H. *Phys. Rev. Lett.* **1990**, *64*, 68−71.
(29) Guedel, H. U.; Furrer, A.; Blank, H. *Inorg. Chem.* **1990**, *29*, 4081−4084.
(30) Furrer, A.; Güdel, H. U.; Krausz, E. R.; Blank, H. *Phys. Rev. Lett.* **1990**, *64*, 68−71.
(31) Aebersold, M. A.; Guedel, H. U.; Furrer, A.; Blank, H. *Inorg. Chem.* **1994**, *33*, 1133−1138.
(32) Moreno Pineda, E.; Chilton, N. F.; Marx, R.; Döfel, M.; Sells, D. O.; Neugebauer, P.; Jiang, S.-D.; Collison, D.; van Slageren, J.; McInnes, E. J.; Winpenny, R. E. *Nat. Commun.* **2014**, *5*, 5243.
(33) Deutsche Forschungsgemeinschaft Molecular Magnetism Research Report: Sessoli, R.; Powell, A. K. *Coord. Chem. Rev.* **2009**, *253*, 2328−2341.
(34) Rinehart, J. D.; Long, J. R. *Chem. Sci.* **2011**, *2*, 2078−2085.
(35) Woodruff, D. N.; Winpenny, R. E. P.; Layfield, R. A. *Chem. Rev.* **2013**, *113*, 5110−5148.
(36) Blagg, R. J.; Ungur, L.; Tuna, F.; Speak, J.; Comar, P.; Collison, D.; Wernsdorfer, W.; McInnes, E. J. L.; Chibotaru, L. F.; Winpenny, R. E. P. *Nat. Chem.* **2013**, *5*, 673−678.
(37) Rinehart, J. D.; Fang, M.; Evans, W. J.; Long, J. R. *J. Am. Chem. Soc.* **2011**, *133*, 14236−14239.
(38) Rinehart, J. D.; Fang, M.; Evans, W. J.; Long, J. R. *Nat. Chem.* **2011**, *3*, 538.
(39) Demir, S.; Zadrozny, J. M.; Nippe, M.; Long, J. R. *J. Am. Chem. Soc.* **2012**, *134*, 18546−18549.
(40) Meihaus, K. R.; Corbey, J. F.; Fang, M.; Ziller, J. W.; Long, J. R.; Evans, W. J. *Inorg. Chem.* **2014**, *53*, 3099−3107.
(41) Komeda, T.; Isshiki, H.; Liu, J.; Zhang, Y.-F.; Lorente, N.; Katoh, K.; Breedlove, B. K.; Yamashita, M. *Nat. Commun.* **2011**, *2*, 217.
(42) Okazawa, A.; Nogami, T.; Nojiri, H.; Ishida, T. *Inorg. Chem.* **2008**, *47*, 9763−9765.
(43) Okazawa, A.; Nogami, T.; Nojiri, H.; Ishida, T. *Inorg. Chem.* **2009**, *48*, 3292−3292.
(44) Shimada, T.; Okazawa, A.; Kojima, N.; Yoshii, S.; Nojiri, H.; Ishida, T. *Inorg. Chem.* **2011**, *50*, 10555−10557.
(45) Okazawa, A.; Shimada, T.; Kojima, N.; Yoshii, S.; Nojiri, H.; Ishida, T. *Inorg. Chem.* **2013**, *52*, 13351−13355.
(46) Murakami, R.; Ishida, T.; Yoshii, S.; Nojiri, H. *Dalton Trans.* **2013**, *42*, 13968−13973.
(47) Nakajima, K.; et al. *J. Phys. Soc. Jpn.* **2011**, *80*, SB028.
(48) Nojiri, H.; Ajiro, Y.; Asano, T.; Boucher, J.-P. *New J. Phys.* **2006**, *8*, 218.
(49) Inamura, Y.; Nakatani, T.; Suzuki, J.; Otomo, T. *J. Phys. Soc. Jpn.* **2013**, *82*, SA031.
(50) Stoll, S.; Schweiger, A. *J. Magn. Reson.* **2006**, *178*, 42−55.
(51) Borrs-Almenar, J. J.; Clemente-Juan, J. M.; Coronado, E.; Tsukerblat, B. S. *Inorg. Chem.* **1999**, *38*, 6081−6088.
(52) Ishida, T.; Murakami, R.; Kanetomo, T.; Nojiri, H. *Polyhedron* **2013**, *66*, 183−187.
(53) Kanetomo, T.; Ishida, T. *Inorg. Chem.* **2014**, *53*, 10794−10796.
(54) Ishikawa, N.; Sugita, M.; Ishikawa, T.; Koshihara, S.-y.; Kaizu, Y. *J. Am. Chem. Soc.* **2003**, *125*, 8694−8695.
(55) Rajeshkumar, T.; Rajaraman, G. *Chem. Commun.* **2012**, *48*, 7856−7858.
(56) Andruh, M.; Ramade, I.; Codjovi, E.; Guillou, O.; Kahn, O.; Trombe, J. C. *J. Am. Chem. Soc.* **1993**, *115*, 1822−1829.
(57) Kahn, M. L.; Sutter, J.-P.; Golhen, S.; Guionneau, P.; Ouahab, L.; Kahn, O.; Chasseau, D. *J. Am. Chem. Soc.* **2000**, *122*, 3413−3421.
(58) Kahn, M. L.; Ballou, R.; Porcher, P.; Kahn, O.; Sutter, J.-P. *Chem.—Eur. J.* **2002**, *8*, 525−531.
(59) Watanabe, R.; Fujiwara, K.; Okazawa, A.; Tanaka, G.; Yoshii, S.; Nojiri, H.; Ishida, T. *Chem. Commun.* **2011**, *47*, 2110−2112.

DOI: 10.1021/acs.inorgchem.5b00300
Inorg. Chem. 2015, 54, 5732−5738